Thermo-photo production of hydrogen using ternary Pt-CeO$_2$-TiO$_2$ catalysts: A spectroscopic and mechanistic study

Uriel Caudillo-Flores [a,b], Irene Barba-Nieto [a], Mario J. Muñoz-Batista [c], Debora Motta Meira [d,e], Marcos Fernández-García [a], Anna Kubacka [a]

[a] Instituto de Catálisis y Petroleoquímica, CSIC.C/Marie Curie 2, 28049 Madrid, Spain
[b] Centro de Nanociencias y Nanotecnología, Universidad Nacional Autónoma de México, Ensenada 22800, México
[c] Department of Chemical Engineering, University of Granada, Av. de la Fuente Nueva S/N, 18071, Granada, Spain
[d] CLS@APS Sector 20, Advanced Photon Source, Argonne National Laboratory, 9700 S. Cass Avenue, Argonne, IL 60439, USA
[e] Canadian Light Source Inc., 44 Innovation Boulevard, Saskatoon, Saskatchewan S7N 2V3, Canada

ARTICLE INFO

ABSTRACT

The gas phase thermo-photo production of hydrogen from methanol:water mixtures was tested using platinum ceria-titania ternary solids. This contribution focusses on the analysis of the role of ceria and the usefulness of combining heat and light sources in order to boost catalytic activity. To this end, we provide a quantitative assessment of thermo-photo activity as well as a detailed characterization of the catalytic solids with emphasis in the use of in-situ X-ray absorption and infrared spectroscopies. The adequate combination of components in the platinum ceria-titania ternary system renders highly active and stable catalysts, maximizing hydrogen production (rate of ca. 45 mmol g^{-1}h^{-1}) for a solid having a 1/2.5 wt% of platinum/ceria supported on titania. The characterization shows that this occurs through a synergetic effect among components of the solids and takes place with a critical role of defects located at the ceria-titania interface and the noble metal component. The cooperative action between components promotes the evolution of specific carbon-containing intermediates (related to the step-wise hole-triggered oxidation of the methanol molecule, decarbonylation of intermediates and the water gas shift) and the concomitant production of hydrogen.

1. Introduction

The increasing human population and industrial activity trigger the need of diversifying the sources of raw materials and to diminish the impact on environment by decreasing or eliminating waste. Catalysis is a central piece of chemical industry, being present in at least one step of countless industrial chemical processes [1]. Thermal (or conventional) catalysis is a well-stablished field of research having impact in the synthesis of high added-value chemical compounds, as well as environmental protection and energy-related processes. An endless challenge for any catalytic process is to decrease cost associated with the catalytic operation parameters (mainly temperature and pressure) as well as to increase the stability/longevity of the material [2]. Photo catalysis makes use of light as the source of the chemical process and finds application in numerous processes in the chemistry field. However, it displays limited application due to typical low reaction rate and quantum efficiency values [3,4]. Thermo-photo-catalysis is a young research field aiming to combine thermal and light energy sources. A main aim within dual thermo-photo catalysis is to decrease or even solve the already discussed weaknesses of the single energy source processes.

Thus, it appears as an attractive path to provide useful (catalytic) alternatives to a significant number of chemical processes of industrial interest [5,6].

In the field of thermo-photo catalysis, a central issue (among others) is how simple and effective is to introduce illumination sources in classical heating set-ups. Such a combination has been shown success in enhancing activity. A net effect is detected in T$_{50}$, T$_{100}$ isoconversion temperature(s) for several chemical processes. As illustrative examples, we can mention the CO oxidation process using Pt-TiO$_2$ [7] dye degradation using defective CeO$_x$/CeO$_2$ powders [8] 2-propanol oxidation using composite CeO$_x$-TiO$_2$ materials [9,10] and oxidation of aromatics (benzene, toluene, xylenes) with Ag/SrTiO$_3$ or CeO$_2$/LaMnO$_3$ catalysts [11,12]. Interestingly, the production of hydrogen through a thermo-photo process has been recently addressed with Ni [13] Co [14] Pt [15] Ru [16] and Pd [17] based catalysts using titania as support. In these three works, results show that light excitation upon a thermal process leads to significant improvements in terms of hydrogen yield as well as stability of the catalysts under reaction conditions.

The physical grounds sustaining the promotion of the activity in the above-mentioned thermo-photo catalytic formulations are nevertheless

unclear. Multiple factors affecting positively catalytic performance of thermo-photo materials can be mentioned here. For metal-promoted titania catalysts, the improved utilization of the UV and visible regions as well as local (localized) electric field and heating by plasmonic are frequently invoked in the literature [16,18,19,20]. In addition, other physical phenomena can be briefly mentioned. In the case of oxide-oxide materials, the interface role together with the handling of anionic vacancies are often mentioned to favor activity [6,8,9,21]. Besides that, significant and general (no matter the nature of the catalytic system) catalytic effects would come out from new surface chemistry connected with behavior differences in presence/absence of light and in turn related to specific reaction steps with participation of excited (directly by light or by interaction with "excited" defects, etc.) species and/or variations in surface coverage(s) [6,7,15,17,20]. All these factors can take place simultaneously and therefore can obscure the understanding of the underlying physico-chemical phenomena determining activity in thermo-photo catalytic processes. Such a scenario calls for further studies.

Noble metal supported on TiO_2 or CeO_2 systems have been shown activity in thermal [22,23] and photo [24,25,26,27,28] catalytic production of hydrogen. Moreover, the effective use of the noble metal-titania general formulation in hydrogen thermo-photo production has been previously noted here [15,16,17]. Nevertheless, to the best of our knowledge, the utilization of mixed ceria-titania supports has not been analyzed in the context of hydrogen thermo-photo (combined energy source) production. This in spite of the fact that the combination of these two oxides has been shown to be among the most active formulations for the thermal reforming of alcohols [29,30]. In addition, such combination has shown to boost strongly the photo catalytic activity of the corresponding bare titania or ceria (alone) based systems [31,32,33,34]. Therefore, the Pt-CeO$_2$-TiO$_2$ catalyst is, to our knowledge, a novel formulation with high potential for hydrogen thermo-photo generation, tested here for the first time. In this context, a first goal is to provide an adequate measurement of the (potential) energy gain when combining thermal and light excitation sources. To do it, we make use of the so-called excess function for both the reaction rate and quantum efficiency observables. This is calculated by subtracting thermo-photo values to the sum of thermal and photo (corresponding) observables. In addition, a complete characterization of the catalysts was performed using microscopy techniques as well as UV–visible, X-ray diffraction, Raman, and microsized X-ray absorption (X-ray absorption near edge structure XANES and extended X-ray absorption fine structure EXAFS) spectroscopies. These techniques proved the structural and electronic properties of the catalytic powders. Particularly, the in-situ analysis under illumination using a X-ray microbeam has been shown to scrutinize the active components exclusively at the surface zone, and thus the part of the catalyst really under simultaneous illumination and contact with the reaction atmosphere at the desired temperature of operation [35]. The study also utilizes infrared spectroscopy to scrutinize the gas–solid interface under reaction (photo, thermal and thermo-photo) conditions to provide information about the reaction intermediates and mechanism. The combination of information coming from these three pieces renders a unique view of the process and allows to highlighting the usefulness of the thermo-photo process with respect to single thermal or photo process, providing at the same a quantitative estimation of the benefits.

2. Experimental

The synthesis of the catalysts was carried out by a combination of techniques. The oxide supports were obtained through a combination of microwave-microemulsion techniques and subsequent calcination. The metal was included in a posterior step using an aqueous chemical reduction technique. The nomenclature of the catalysts was: Pt/xCeO$_2$-TiO$_2$. The × (x = 1, 2.5 and 5) gives the weight percentage (measured by chemical analysis) of the cerium-containing phase expressed as CeO$_2$.

Single oxide supports were used as references in the Pt/TiO$_2$ and Pt/CeO$_2$ catalysts. All catalysts contain a 1 wt% of noble metal. Samples were fully characterized using ex and in-situ techniques and subjected to reaction for gas-phase hydrogen thermo-photo production. Catalytic activity was measured using reaction rates (normalized per surface area) and quantum efficiency observables following IUPAC rules. To obtain the quantum efficiency equation 1 is used:

$$QE(\%) = 100 \times \frac{2 \times r(\text{mol m}^{-2} \text{ s}^{-1})}{e^{a,s}(\text{Einstein m}^{-2} \text{ s}^{-1})} \tag{1}$$

In this equation, r is the reaction rate and $e^{a,s}$ the average local superficial rate of photon absorption. [36]. The factor two considers the requirement of two electrons per hydrogen molecule. Full details of all procedures and techniques can be found at the supporting information file.

3. Results and discussion

3.1. Catalytic results

As mentioned, the activity of the ternary Pt-CeO$_2$-TiO$_2$ catalysts and reference systems is here analyzed using the reaction rate (Fig. 1) and quantum efficiency (Fig. 2) observables as well as the corresponding excess observables (described in equations S1/S2) as a function of the reaction temperature under dark/illumination conditions. The role of the alcohol is essential as a decay of more than two orders of magnitude are obtained in the two observables using exclusively water. The excess values measured the gain obtained by combining light and heat sources with respect to the (additive) use of the two sources separately. As can be seen in Figs. 1 and 2, the use of temperature alone renders rather limited activity below 200 °C irrespective of the sample here utilized. Contrarily, light excitation triggers some activity and room temperature. Moreover, combining the two energy sources provides significant activity already at 120 °C, with a clear enhancement of activity around/above 200 °C. The stability of selected materials under long-term operation was also tested and (catalytic and physico-chemical characterization of post-reaction samples) results presented in Figure S3.

As described in the introduction section, Pt presence is essential to obtain significant activity in both thermo and photo production of hydrogen [15–17]. The presence of ceria in the ternary photocatalysts further enhanced activity in all cases tested (e.g. irrespective of excitation energy nature and temperature of testing) with respect to the pure oxides references (pure ceria-based Pt-promoted catalyst is not presented as shown reaction rates from 5 to 8 times lower than the Pt/TiO$_2$ reference). Moreover, maximum activity is reached with the Pt/2.5CeO$_2$TiO$_2$ material irrespective of the energy source or reaction temperature. This material provides rather high activity (reaction rate up to 45 mmol g^{-1}h^{-1}) and an enhancement ratio with respect to Pt/TiO$_2$ going from 1.2 to 1.8 times (reaction rate) or from 1.6 to 2.1 (quantum efficiency) as a function of the temperature. Note than the differences in all observables support the positive effect of ceria in the activity of the Pt-promoted titania-based system.

Another important piece of information for the analysis of the activity will come from the detailed analysis of the excess functions. The bottom part of Figs. 1 and 2 provides a quantitative measurement of the beneficial effect taking place when using the energy sources simultaneously. The excess function reaches the maximum at 240 °C independently of the observable utilized to measure it. Clearly, over this temperature the thermal component of the reaction dominates the catalytic response of the samples. For the quantum efficiency (as well as the reaction rate), the maximum excess value occurs at 240 °C, and corresponds to the Pt/2.5CeO$_2$TiO$_2$ material, reaching a value of ca. 49%. This excess function is significantly larger than the one previously reported for noble metal (Pt, Pd, Ru) particles supported over bare titania systems [15–17]. Thus, this ternary material renders a highly active
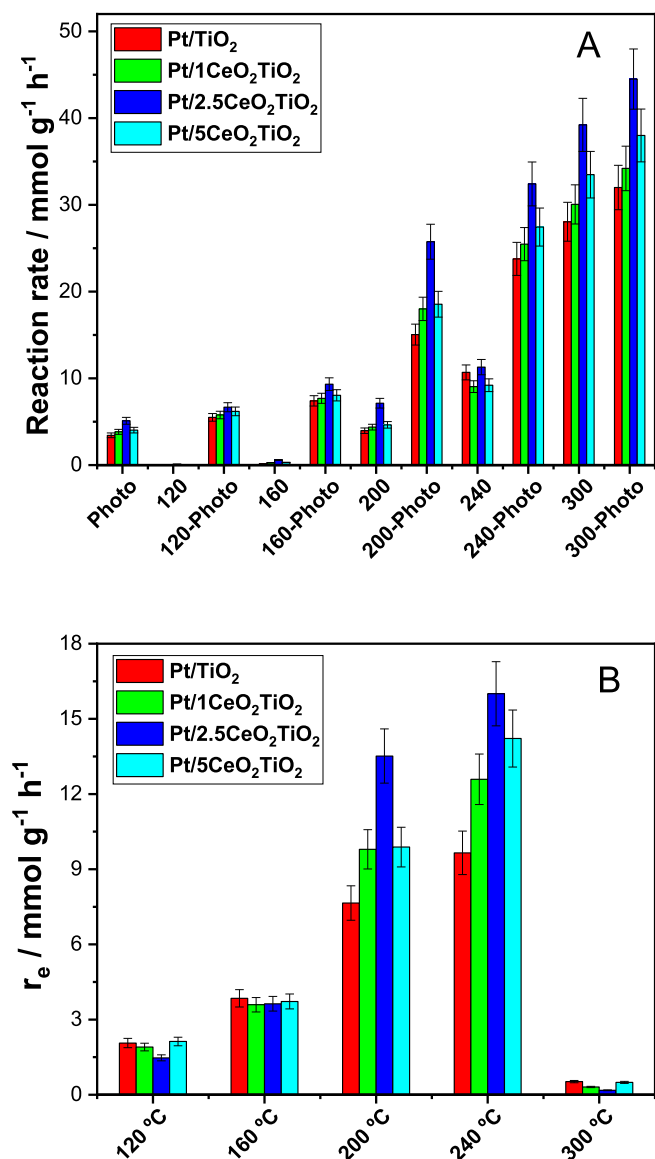
Fig. 1. Reaction rate (A) and excess rate (equation S1; B) for the sample and reference materials as a function of the temperature and dark/illumination conditions. Thermal (reaction temperature indicated as label), photo (at room temperature), and thermo-photo ("temperature-Photo" used as label) conditions are tested in the figure.
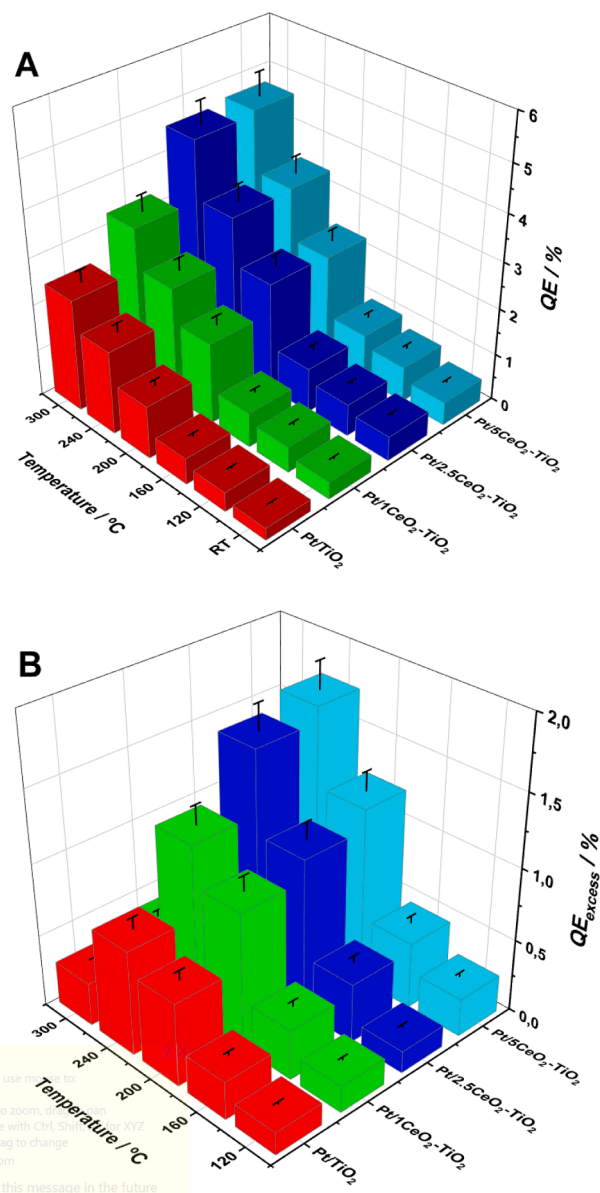

Fig. 2. Quantum efficiency (A) and quantum efficiency excess (B) for the sample and reference materials as a function of the temperature under illumination conditions.

system as measured by both reaction rate/quantum efficiency. The synergy measured is ca. 50%, or, in other words, nearly 1.5 times hydrogen yield (from the simple additive result) when we combined the two energy sources. The energy balance of the reaction (see supporting information for calculation details) is positive when comparing the combined use of energy sources with the bare sum. Using the rates presented in Fig. 1, we measured an energy profit of about 19% (worst case, Pt/TiO$_2$) to 34% (best case, Pt/2.5CeO$_2$TiO$_2$) with respect to the additive combination of energy sources. It is also important to stress the fact that the best sample (Pt/2.5CeO$_2$TiO$_2$) provides stable operation for hydrogen photo-production under repeated experiments (Figure S3).

3.2. Characterization of the initial stage of the catalysts

The characterization here carried out combines classical (ex situ) as well as in-situ studies of the photo-catalysts. Our materials are high surface area catalysts, with the BET area presenting a value of ca. 150 m^2 g^{-1} for Pt/TiO$_2$ reference, and decreasing values up to ca. 95 m^2 g^{-1} for

the ternary sample having the highest quantity of ceria (Table 1). As shown by the opposite trends (vs. ceria content) detected in pore volume and size values, this may occur by partial occlusion of the smallest mesopores of titania. This in turn takes place by surface deposition of the minor components (particularly ceria) of the ternary systems. The parallel structural characterization was initially performed with a combination of X-ray diffraction (XRD) and Raman spectroscopy. As can be seen in Fig. 3A, XRD patterns essentially show the presence of the anatase polymorph of titania (JCPDS card 21–1272; I4$_1$/amd space group) [37]. Using the Scherrer equation, the primary particle size of the anatase component is between 10.5 and 12 nm for all samples. Similarly, the shape of the Raman spectra (Fig. 3B) provide evidence of the anatase polymorph presence, displaying peaks at ca. 143, 395, 515 and 636 cm^{-1} [38]. On both techniques there are additional weak peaks ascribable to the presence of other phases. Of particular interest, XRD patterns detect the presence of the fluorite phase of ceria (JCPDS card 87–0792; Fm3m space group) from a content of 2.5 wt% and a weak peak at ca. 31 degrees indicating brookite [37,39]. Raman points out the

Table 1
Surface area, pore volume, pore size and band gap energy for sample and reference systems.[a.]

Catalyst	BET surface area ($m^2 g^{-1}$)	Pore volumen ($cm^3 gr^{-1}$)	Pore size (nm)	Band Gap (e⁻V)
Pt/TiO$_2$	156.5	0.262	6.0	3.21
Pt/1CeO$_2$TiO$_2$	120.1	0.245	7.3	3.18
Pt/2.5CeO$_2$TiO$_2$	114.4	0.243	7.6	3.20
Pt/5CeO$_2$TiO$_2$	94.8	0.235	8.8	3.19
Pt/CeO$_2$	128.5	0.275	8.0	2.81

Average standard error: BET area: 3.6%; pore volume/size 5.4%; band gap: 0.03 eV.

presence of rather minor contributions of brookite (201 cm^{-1}) and barely detected ceria by the characteristic peak at ca. 475 cm^{-1} [31,40]. As expected, for ternary samples these two bulk-sensitive techniques signals were dominated by the major (by weight percentage) anatase phase.

In order to gain insight about the minor phases, a detailed microscopy study of the materials was carried out. In Fig. 4 we present micrographs for three representative samples, the Pt/TiO$_2$ reference, and the Pt/2.5CeO$_2$TiO$_2$ and Pt/5CeO$_2$TiO$_2$ samples. In all cases well-defined, round-shaped metallic particles can be clearly observed. They are well dispersed over the whole surface of the reference and ternary materials. The figure also includes (right hand side of the figure) the primary particle size distributions of the noble metal component. The distributions are relatively narrow, with a moderate skewedness (higher for the higher Ce content catalyst) to larger particle sizes from the average value. The noble metal average primary particle size values are reasonable similar among samples, with nearly equal values (3.4–3.5 nm) for the Pt/TiO$_2$ reference and the Pt/2.5CeO$_2$TiO$_2$ sample, and a slightly higher one (3.9 nm) for the Pt/5CeO$_2$TiO$_2$ catalyst. The chemical deposition method is thus rendering a rather stable noble metal particle size over the set of catalysts studied. The contact between components of the catalysts is analyzed in the high-resolution micrographs presented in Fig. 5 and Figure S4,S5. In Fig. 5/Figure S4, anatase nanoparticles of ca. 10 nm and well-defined rounded shape are observed, dominantly presenting the most stable crystallographic plane (e.g. (1 0 1)). For ceria-containing samples, ceria is detected in significantly smaller entities, as expected by the corresponding weight percentage of the catalysts. In the micrographs we observed the exposure of typical, most-stable fluorite surfaces (dominated by the (1 0 1) and (2 2 0) planes) [31,33,41]. The microscopy study shows the good dispersion of the nanosized ceria particles, with some tendency to be in neighboring zones near the noble metal. The energy dispersive X-ray spectroscopy maps (Figure S5) further confirm the close contact between the metal and the lanthanide components.

The basic characterization is completed using UV–visible spectroscopy. The corresponding spectra are presented in Figure S6. Except for the Pt/CeO$_2$ catalyst, we observed rather small differences between the displayed spectra. This comes out from the dominant presence of the similar (according to XRD/Raman) anatase phase present in the ternary systems. The UV–visible spectra show the characteristic s-type shape dominated by the band gap feature of the semiconductor components (anatase in the case of the ternary systems). Considering that anatase is an indirect gap semiconductor, [3] we calculate the corresponding values for the band gap energy. These values are collected in Table 1. As expected, an essentially constant magnitude of ca. 3.20 eV is obtained from the Pt/TiO$_2$ reference and ternary materials. This is a typical result for the anatase phase, in agreement with the structural characterization of the materials [31,33,38]. For Pt/CeO$_2$, with ceria being also an indirect gap semiconductor [3] the band gap value goes to ca. 2.8 eV. Also, the analysis of the valence band (Figure S7) provides solid evidence that the ternary systems not only display essentially equal values of the band gap energy (Fig. 6) but also rather similar energy position(s) for valence and conduction bands.

In short, the structural and electronic basic characterization of the calcined solids indicates limited differences among ternary systems,

mostly related to a decrease of surface area as well as the increase of ceria particle size with the increase of the ceria content along the sample series. We also note that valence/conduction band positions and band gap energy of post-reaction powders do not vary (within experimental error) with respect to the initial stage for all samples (results not shown).

3.3. In-situ study of the catalysts under reaction conditions

The response of the system under reaction conditions was studied by a combination of characterization techniques. The behavior of the catalysts was analyzed using X-ray absorption techniques while the gas–solid interface was studied using infrared spectroscopy. X-ray absorption was applied to the Ti K and Pt and Ce L$_3$-edges under reaction conditions at dark and illuminated conditions. In the case of the noble metal, Fig. 6 collects XANES and EXAFS spectra of selected samples. The Pt L$_3$-edge study particularly focusses in the comparison between the Pt/TiO$_2$ reference and the most-active Pt/2.5CeO$_2$TiO$_2$ sample, scanning results under illumination over the temperature range of activity data presented in Figs. 1 and 2. The comparison of XANES data with a Pt foil reference (Fig. 6A, C) indicates the presence of a metallic phase. From the microscopy study we learned that this is the initial state of the noble metal component, a fact also described using XAS by other authors in Pt-promoted titania-based photocatalysts for hydrogen photo-production [42]. However, the current XANES study demonstrates beyond doubt the stability of the metallic chemical state under all reaction conditions here tested. The inset plots in these figures (6A,C) show only minimal differences in XANES white line shape and thus, electronic state, as a function of the temperature for all samples. The Fourier transform of the EXAFS signal(s) at room temperature is also included in the Figure (panels B,D) and compared with the Pt foil. The lower intensity (for the first four shells) with respect to the foil demonstrates the presence of nanoparticles with spherical or nearly spherical-type shape [43] Fitting of the EXAFS signals (results shown in Figures S8 and S9) indicates a 1st shell coordination number of 10.4 ± 0.9 and 10.5 ± 1.0 for, respectively, the Pt/TiO$_2$ reference and the most-active Pt/2.5CeO$_2$TiO$_2$ sample. For spherical-type particles these numbers correspond to particles of ca. 3.5 nm [44] in full agreement with microscopy the results presented in Fig. 4. Interestingly, Figures S8 and S9 also provide conclusive proof of the stability of the metallic particles under reaction conditions. The comparison of the room temperature of the initial and post-reaction Pt L$_3$-edge Fourier transform spectra shows minimal differences, a result consistent with the activity stability of the noble metal component.

The Ce L$_3$-edge XANES signal was also measured. Fig. 7 collects data for the Pt/2.5CeO$_2$TiO$_2$ and Pt/5CeO$_2$TiO$_2$ samples and the 5CeO$_2$TiO$_2$ support. Oxide-type reference for the Ce^{4+} and Ce^{3+} oxidation states are also included. As it can be seen in the figure, the fluorite Ce^{4+} oxide shows a rather characteristic shape, with a shoulder near the edge and a while line split in two well-defined peaks (located at ca. 5728.5 and 5735 eV). This is characteristic of the mixed valence ground state of the Ce^{4+} oxidation state. Contrastingly, the Ce^{3+} oxidation state presents a single peak (white line at ca. 5724 eV) in this region [39,43]. This fact has been used to provide a measure of the reduced Ce fraction (Ce^{3+}) using the difference spectra. The scale is calibrated utilizing the difference between the two references. The value corresponding to the
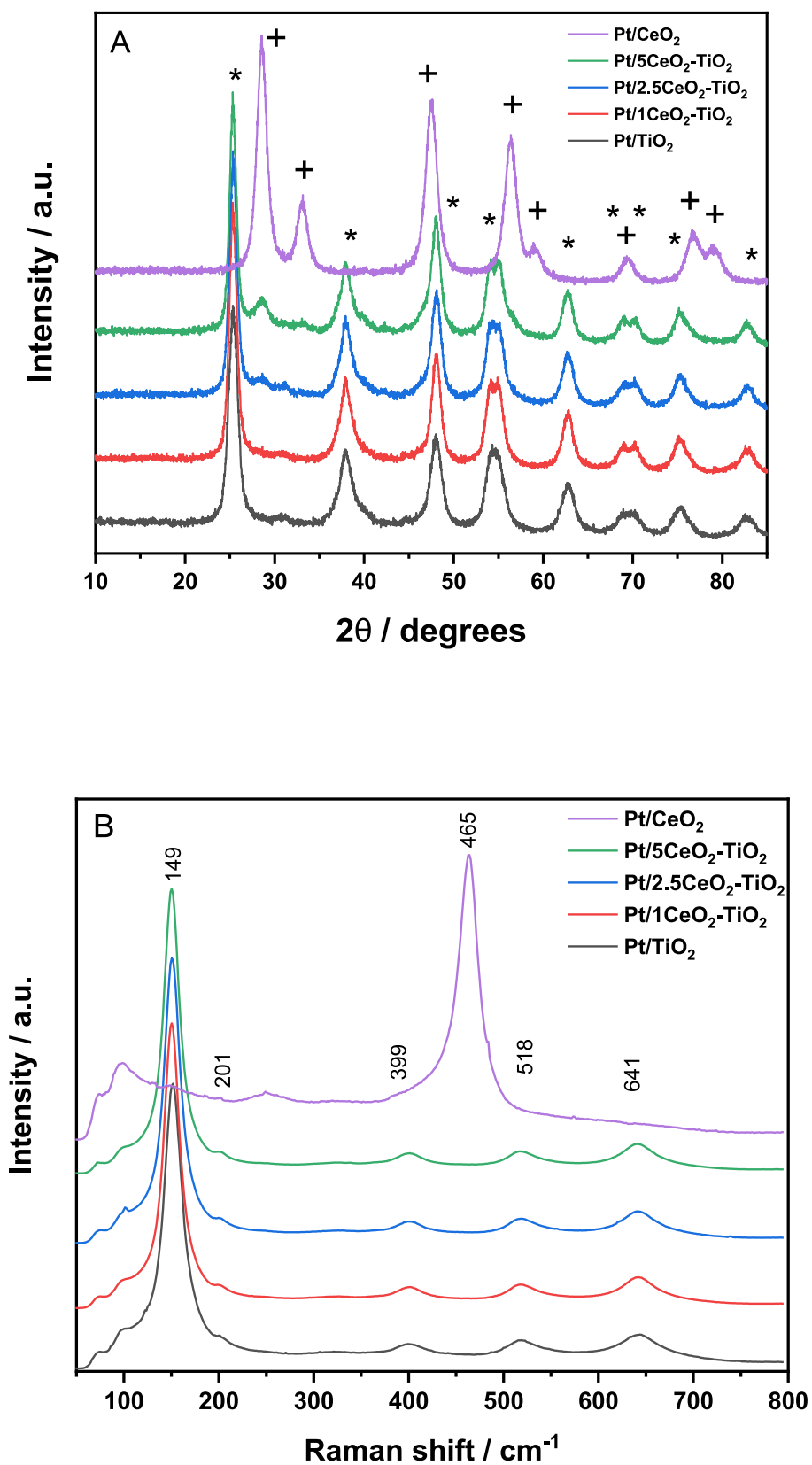
Fig. 3. XRD profiles (A) and Raman spectra (B) for the samples and reference materials. Anatase (*) and Fluorite (+) reflections are marked in the XRD profiles.

difference between the main XANES peaks of the Ce^{4+}/Ce^{3} reference spectra is assigned to a 100% of reduced Ce species [43,45]. Applying this well-known methodology, we calculated the fraction of Ce^{3+} present under reaction at the temperatures selected for catalytic testing.

The upper, right hand plot of Fig. 7 collects this information. As previously observed in composite catalysts having ceria-titania supports, the fraction of reduced Ce species decreases with the ceria content of the binary oxide [29,31,33]. This can be expected considering the behavior
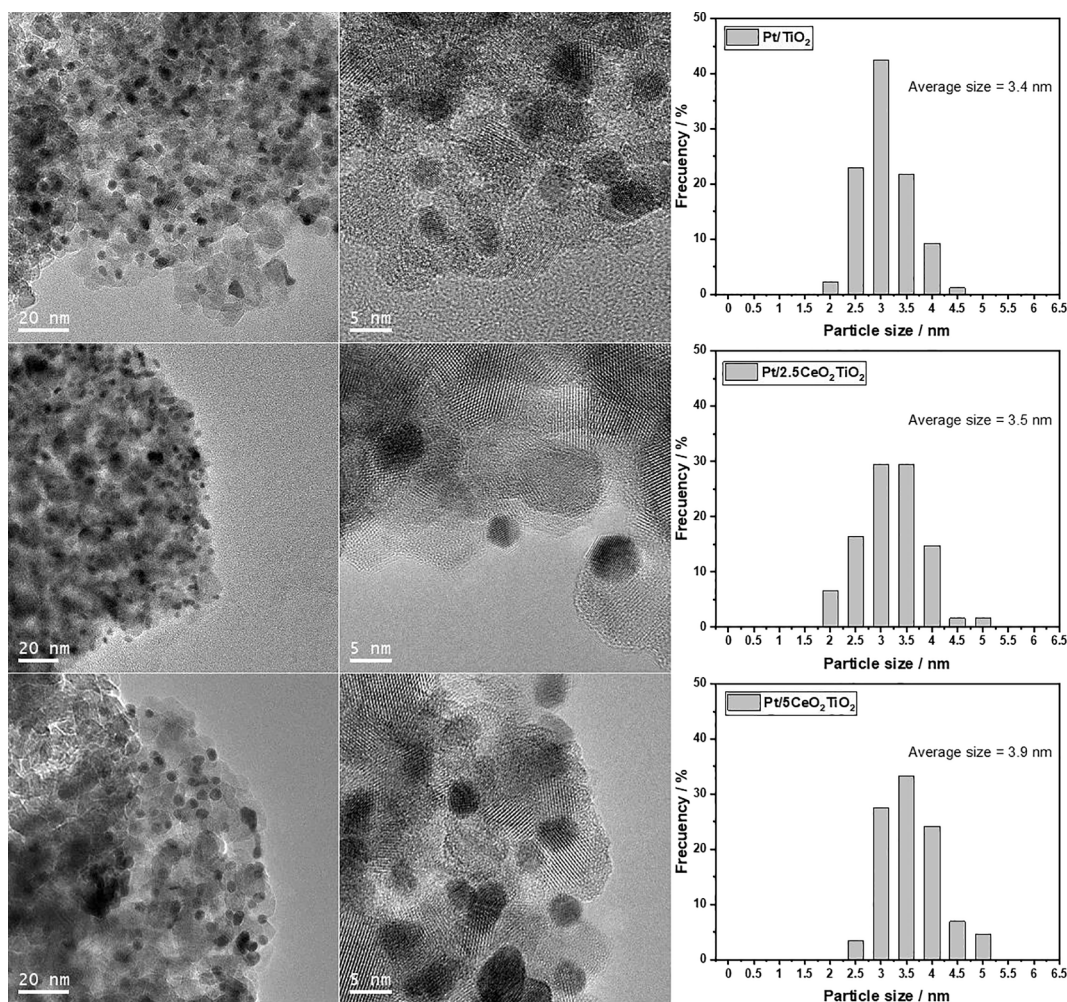
Fig. 4. Low (A-C) and high (D-F) magnifications TEM images and noble metal particle size distributions (G-I) for selected samples. Sample name is included in the metal particle distribution plot.

of the primary particle size of the Ce-containing phase along the series of samples and the decreasing fraction of Ce in contact with the titania component as the lanthanide content grows (see below). In our case, at room temperature (result relevant for pure photocatalysis) this goes from ca. 65–70% for the Pt/1CeO$_2$TiO$_2$ (result not shown) and Pt/2.5CeO$_2$TiO$_2$, to about ca. 40% in the Pt/5CeO$_2$TiO$_2$ case. Curiously, this fraction is essentially stable as a function of the temperature for samples with a ceria content below 2.5 wt% and increases for the highest loading tested, 5 wt%. The stability of the signal for the Pt/2.5CeO$_2$TiO$_2$ sample is also observed at dark (conditions) while the same increasing trend is detected at dark conditions for the Pt/5CeO$_2$TiO$_2$ case catalyst (Figure S10). So, the difference in reduced Ce fraction between the samples with loadings of ceria above and below 2.5 wt% is essentially commanded by temperature. Fig. 8 also compares the highest loading ceria ternary sample (Pt/5CeO$_2$TiO$_2$) and corresponding binary support (5CeO$_2$TiO$_2$). This comparison allows to concluding that the progression in the reduction of Ce is (dominantly) driven by the interaction between the fluorite and anatase phases, with lack of significant effects related to light and noble metal presence. Summarizing, the X-ray absorption (together with our previous, ex-situ analyses) of the solids indicates that the Pt metal phase is rather similar among the ternary (and reference) samples while differences are encountered in the reduced Ce fraction. This fraction decreases as the Ce content of the ternary system increases, as an effect exclusively ascribable to the interaction with anatase. The latter has been previously noted in binary ceria-titania powders and it is here demonstrated for the first time under thermo-photo conditions

[29,31,33] Note that the parallel analysis of the Ti K-edge (see Figure S11 for representative results) does not show changes of the Ti oxidation state as a function of the temperature or illumination.

In summary, the ceria-titania interaction controls the Ce^{3+} fraction (and concomitant generation of oxygen vacancies in the fluorite phase [39]) irrespective of the dark or illuminated conditions of the sample under reaction. As the titania particle size is constant through the series of catalysts (see XRD/TEM results; Figs. 3-5), this reduced cerium fraction is a function of the ceria primary particle size. Ce cations without interaction with titania maintain the characteristic Ce^{4+} oxidation state of the fluorite structure, justifying the trend(s) observed in Fig. 7 at room temperature (initial state of the samples) as a function of the ceria content of the ternary catalysts. Under reaction conditions, the temperature alters the Ce oxidation state exclusively for the highest Ce loading. So, the oxidation state alteration occurs (dominantly) for cerium cations without direct contact with anatase. There is lack of detection for any combined effect of light and temperature in the oxidation state and structural properties of the noble metal and cerium oxide components of the ternary catalysts (Figure S10).

The gas–solid interface behavior under reaction conditions was interrogated using infrared spectroscopy. We start the analysis of the results at room temperature. Figures S12 to S15 give difference spectra (details of the procedure described at the supporting information file) for the Pt/TiO$_2$ reference and all ternary samples, both at dark and under illumination conditions. The higher wavenumber region displays C–H stretching models ascribable to methanol (C–H contributions at
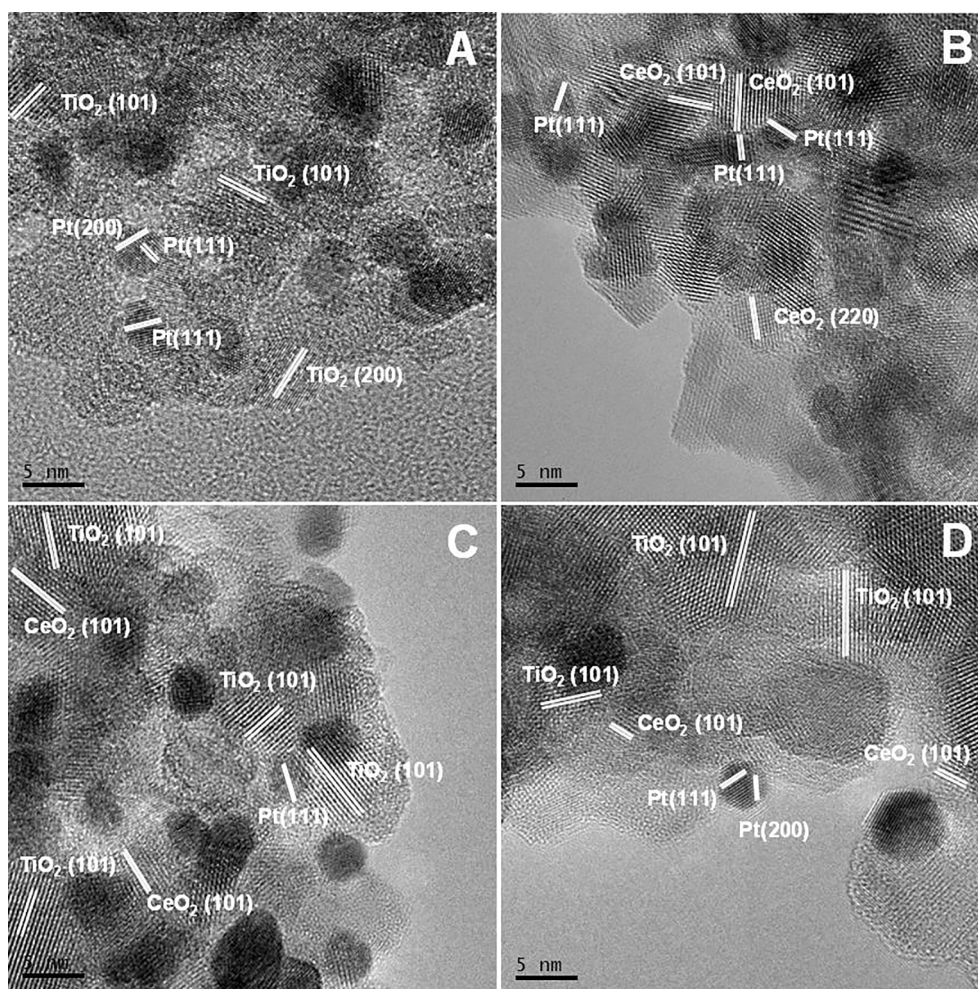
Fig. 5. High resolution TEM images for: A) Pt/TiO$_2$, B) Pt/CeO$_2$, C) Pt/2.5CeO$_2$-TiO$_2$, and D) Pt/5CeO$_2$-TiO$_2$.

2947–2950/2838–2842 cm^{-1}) and methoxy (2920–2930/2819–2826 cm^{-1}) species. These peaks are observed together with characteristic C-O stretching (1033–1035 cm^{-1}) for atop and, likely, (1100–1110 cm^{-1}) for bridge bonded species. However, other surface species can contribute to the last peak [46,47]. Additional strong peaks at ca. 1550–1556/1350–1365 cm^{-1} correspond to bridged-bonded carboxylate (typically formate) species [48,49,50,51]. Presence of other carboxylates/carbonates species are also detected by the broad band at ca. 1409–1420 cm^{-1}. Particularly evident under illumination conditions are peaks at ca. 2960, 1700–1780, 1440–1450, 1360–1380, and 1255–1270 cm^{-1}, which can be ascribed to methylformate type species [50,52]. Ce-containing samples display an increase of the overall intensity in the 1600–1000 cm^{-1} region under both dark and illumination conditions, indicating that methylformate and bidentate formate and, in general, formate formation is favored for the ternary systems. On the other hand, the spectra also detected the existence of carbonyl species on Pt, corresponding to signals centered at 2028–2030 and 2058–2065 cm^{-1} frequencies. Both are assigned to atop carbonyl moieties. The higher/lower wavenumber counterparts would be at near flat surfaces of small particles and their kinks and edges [53,54]. The first carbonyl species is reactive under illumination conditions. Note the absence of carbonyl species adsorbed on titania (ca. 2175–2120 cm^{-1}; see ref. [55]), not detected using infrared. Thus, CO is generated near the noble metal entities and quickly sticks onto the noble metal surface.

Under illumination, the hole-related charge carrier species attacks the sacrificial alcohol molecule. This phenomenon occurs with generation of progressively oxidized species and formation of formaldehyde

and formic acid entities. These steps are described in equations 1 and 2. The process would further progress from formic acid to CO$_2$ with an overall reaction such as $CH_3OH + H_2O \xrightarrow{6h^+} CO_2 + 3H_2$ [28,31,56,57,58]. In parallel, protons (and finally hydrogen; $2H^+ \xrightarrow{2e^-} H_2$) are produced in each step of the reaction, rendering thus a step-like reforming type mechanism with the alcohol playing the role of a sacrificial entity. Note that in equation 1 hydrogen comes from the alcohol molecule while in equation 2 the source is (formally) the water molecule. This mechanism is consistent with the detection of methanol/methoxy species as well as formate (and other carboxylates) species as main surface species [26,59,60].

$$CH_3OH \xrightarrow{2h^+} CH_2O + 2H^+ \qquad (1)$$

$$CH_2O + H_2O \xrightarrow{2h^+} CHOOH + 2H^+ \qquad (2)$$

In our case, we additionally detected methylformate species, formed by interaction of adsorbed methanol/methoxy and formic acid/formate species (equation 3) [49,52]. Also, CO species over Pt were detected. CO formation can occur through the decomposition of aldehyde and/or carboxylate type species (equations 4 and 5, respectively) [49,56]. These steps occur with evolution of hydrogen atoms coming from the alcohol molecule. Interestingly this molecule does not evolve at dark conditions but progress under illuminated conditions (negative peak as IR results are shown as difference spectra) at room temperature. As shown in Table 2, and in the infrared spectra (Figures S12-S15), CO is not detected at the gas phase at room temperature (dark/illuminated
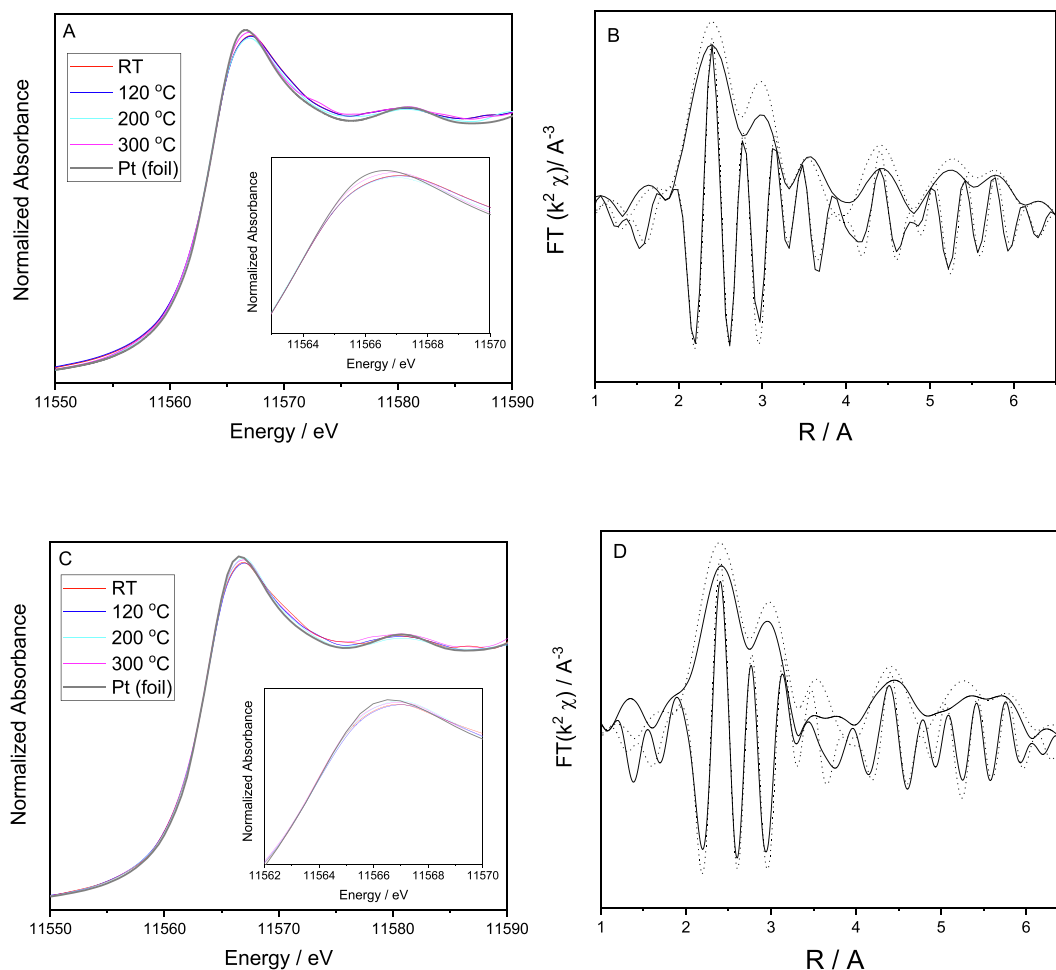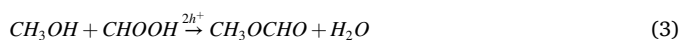
Fig. 6. Pt L$_3$-edge XANES (A,C) and EXAFS (B,D) spectra obtained under illumination as a function of reaction temperature for Pt/TiO$_2$ (A,B) and Pt/2.5CeO$_2$TiO$_2$ (C, D) samples. Spectra obtained at surface position. XANES plots include an inset for the white line region. EXAFS plots show the k^2 weighted module and imaginary part of the samples and Pt foil (the latter as dotted lines).

conditions), indicating the existence of a water gas-shift type reaction step (equation 6) promoted by the metal component [28,56]. Due to the high surface population of the carboxylate species in all samples, the CO generation at room temperature seems to come mainly from equation 5. The water gas shift step promotes the generation of hydrogen from the one ascribed to the main reforming-type mechanism only under illumination (at room temperature), and it is intimately linked with the decarbonylation steps of the main intermediates (formaldehyde and formic acid, the latter predominating here). On the other hand, ceria promotes (particularly for the Pt/2.5CeO$_2$TiO$_2$ sample) both the formation of surface carboxylates (equations 2/3) and the decarbonylation reaction (equation 5), influencing the water gas shift reaction (equation 6; Figures S12-S15). As the adsorbed species are clearly present over the titania surface (or noble metal in the CO case), presenting rather similar frequencies in presence/absence of ceria, the influence of the lanthanide component would proceed through the change of the electronic behavior of the ternary systems. This is further discussed below.

$$CH_3OH + CHOOH \xrightarrow{2h^+} CH_3OCHO + H_2O \quad (3)$$

$$CH_2O \xrightarrow{2h^+} CO + 2H^+ \quad (4)$$

$$CHOOH \xrightarrow{2h^+} CO + OH^- + H^+ \quad (5)$$

$$CO + H_2O \underset{\rightleftharpoons}{\overset{2h^+}{}} CO_2 + H_2 \quad (6)$$

To study the temperature and combined light/temperature effects, we present results at 160 °C (Figures S16-S19) and 240 °C (Figs. 8-11). The first temperature shows the initial stage of the temperature alone reaction while the second corresponds to the one showing maximum synergistic effects between light and temperature. Parallel data considering the (gas-phase) production of carbon-containing molecules and hydrogen vs. temperature of reaction is summarized in Table 2. Changes with temperature are gradual. Most significant changes from room temperature concern the appearance of formaldehyde surface species, indicated by peaks at the C–H region (ca. 2737–2745 cm^{-1}). These species are adsorbed on titania [61]. So, changes in the surface coverage of the dominant methoxy/carboxylate species allow the existence (or significant increase) of aldehyde-type species (equation 1) under reaction at temperatures (particularly above 160 °C). The decarbonylation of these new species (equation 4) triggers an increase of the CO at the gas phase according to Table 2. Modest but clear influence of light can be noticed for this particular step. Under light both the presence of CO gas detected by IR (Figs. 8-11) and chromatography (Table 2) is further increased. Overall, the parallel increase of all aldehyde/carboxylate species and, also, of the adsorbed CO consumption indicate that the increase of activity is mostly driven by powering the reaction path going from carboxylates to CO (equation 5) and the subsequent water gas shift reaction (equation 6). The combination of these two types of reactions is responsible of the big increase in the CO to CO$_2$ ratio as well as the H$_2$ vs. (CO + CO$_2$) ratio detected in Table 2 when confronting dark and illumination conditions at the same temperature.
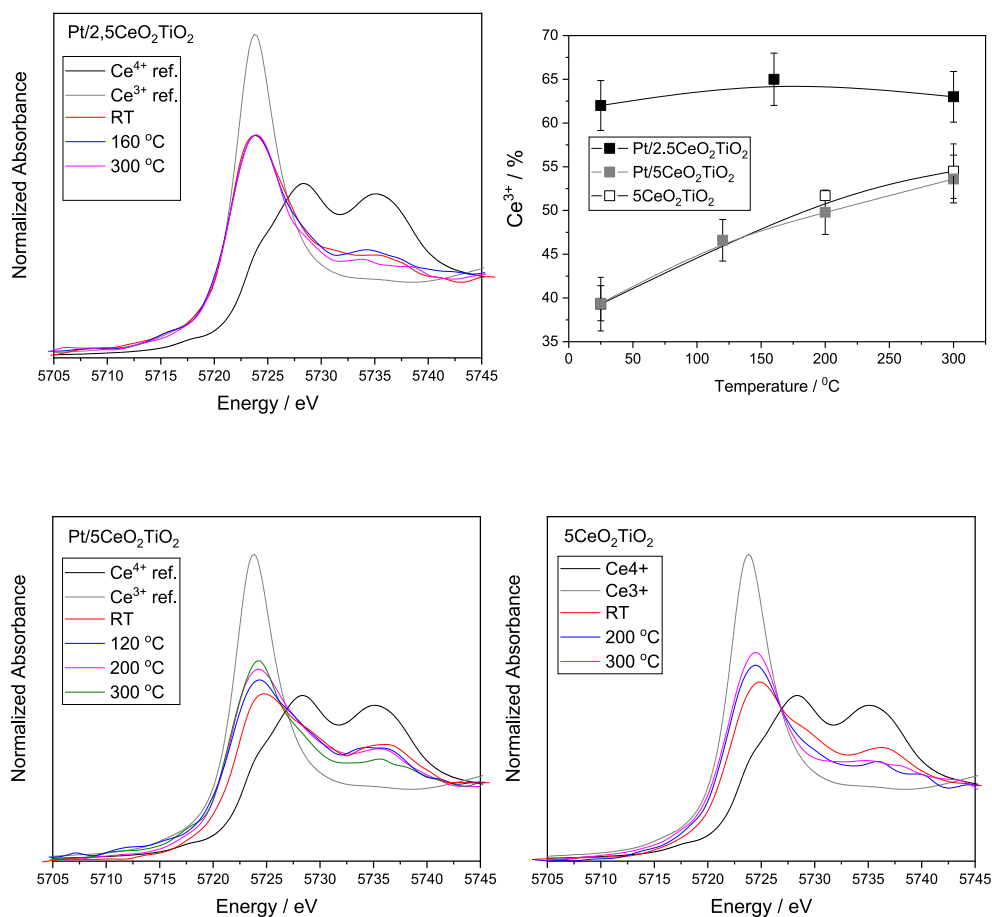
Fig. 7. Ce L$_3$-edge XANES spectra obtained under illumination as a function of the temperature for selected samples and supports. Spectra obtained at surface position. Ce reference spectra (Ce^{4+}; CeO$_2$ and Ce^{3+}; CeAlO$_3$) at room temperature are also presented. At the upper, right corner, the figure includes a panel showing the fraction of Ce^{3+} species present on the samples as a function of the reaction temperature. See text for details.
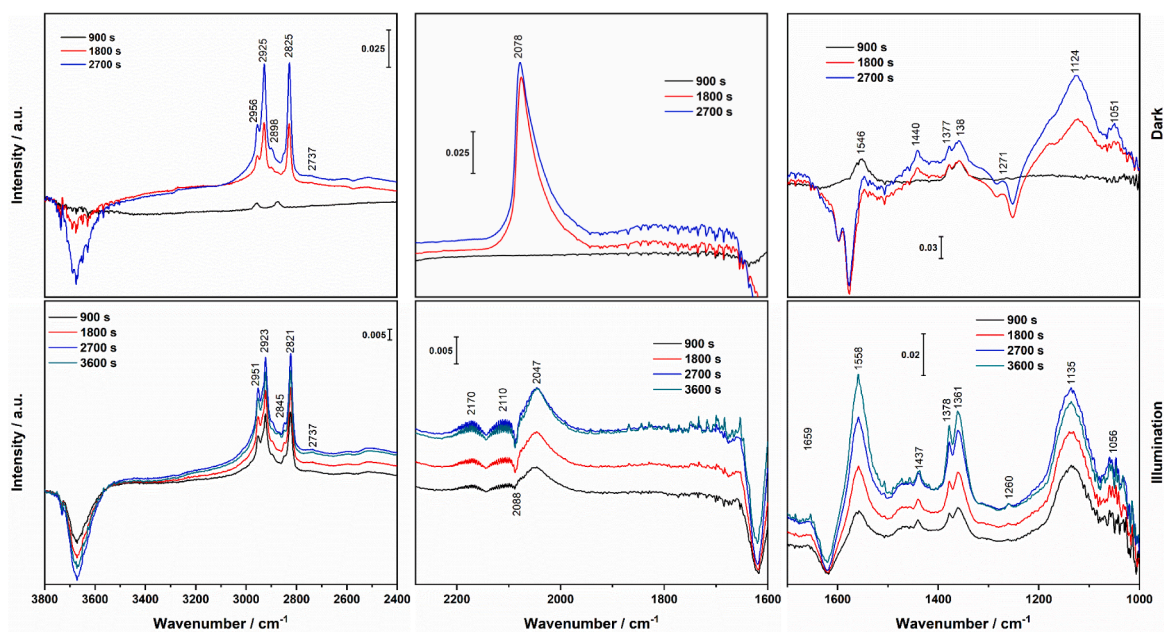

Fig. 8. DRIFT In situ spectra obtained under reaction conditions at 240 °C with the Pt/TiO$_2$ sample: dark (top panel) and illumination (bottom panel) conditions.

Table 2
Molar ratios between reaction products obtained using ternary and reference catalysts.

Temperature-Reaction	Pt/TiO$_2$		Pt/1CeO$_2$TiO$_2$		Pt/2.5CeO$_2$TiO$_2$		Pt/5CeO$_2$TiO$_2$	
	Molar Ratio[a]							
	CO/CO$_2$	H$_2$/CO$_2$ + CO	CO/CO$_2$	H$_2$/CO$_2$ + CO	CO/CO$_2$	H$_2$/CO$_2$ + CO	CO/CO$_2$	H$_2$/CO$_2$ + CO
Photo	0.0	1.6	0.0	2.4	0.0	2.7	0.0	2.5
120	_[b]	_[b]	_[b]	_[b]	_[b]	_[b]	_[b]	_[b]
120-Photo	0.1	2,3	0.1	3.1	0.1	3.2	0.1	3.2
160	_[b]	_[b]	0.0	0.1	0.0	0.1	0.0	0.1
160-Photo	0.3	2.4	0.3	3.2	0.4	3.4	0.3	3.2
200	0.2	0.5	0.1	0.5	0.1	0.7	0.2	0.7
200-Photo	0.9	1.9	0.7	2.8	0.8	3.3	1.1	2.7
240	0.6	0.8	0.8	0.9	0.9	1.0	0.6	1.1
240-Photo	2.0	1.5	1.0	1.8	2.3	2.4	1.9	2.3
300	0.9	1.4	0.9	1.9	0.9	2.3	0.8	2.1
300-Photo	2.3	1.4	1.2	1.6	2.2	2.0	1.7	2.2

Average standard error: CO/CO$_2$ ratio 8.1%; H$_2$/(CO + CO$_2$) 10.6%.
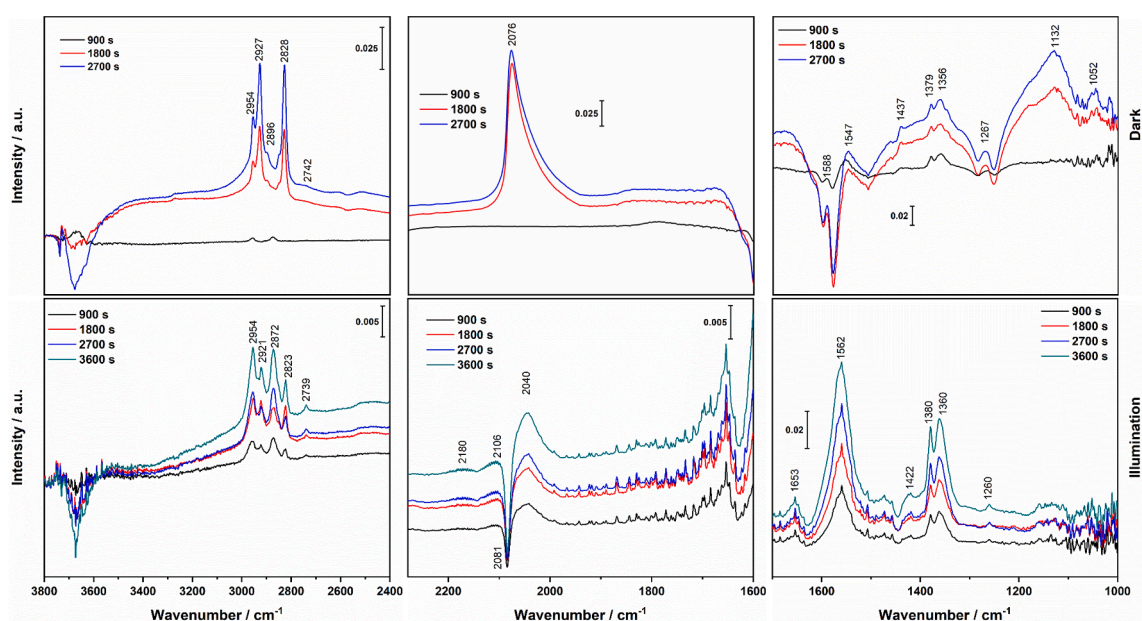Negligible activity.

Fig. 9. DRIFT In situ spectra obtained under reaction conditions at 240 °C with the Pt/1CeO$_2$TiO$_2$ sample: dark (top panel) and illumination (bottom panel) conditions.

In short, the ternary systems are rather similar in terms of the structural and electronic properties, with main changes of catalytic importance related to the fraction of reduced Ce species directly interacting with the anatase support (e.g. having an oxidation state not affected by light and/or temperature under reaction conditions). This reduced Ce fraction is maximized for the Pt/2.5CeO$_2$TiO$_2$ sample. Photoluminescence experiments (Figure S20) indicates the efficient charge carrier handling properties displayed by the ternary system. As well-known, the noble metal acts as an electron sink, decreasing charge recombination [3,28]. Also, ceria is shown to further decrease charge recombination as an effect of electron trapping by anion vacancies associated to Ce^{3+} species [31,62]. Pt and Ce works cooperatively under illumination according to the photo-luminescence results. The mechanism of reaction goes through several carbon-containing intermediates adsorbed onto anatase, followed by the water gas shift onto (or with critical role of) the noble metal. Ceria particularly promotes the generation of carboxylate species (formate and methylformate, equations 2 and 3) and subsequent CO formation (equation 5) species and, likely, the evolution of the last species through the water gas shift reaction (equation 6). On the other hand, light (at temperatures above 160 °C) strongly promotes the surface presence of formaldehyde type species

(equation 1) and the transformation of the higher wavenumber CO species (a species adsorbed at metal sites near ceria) and its consumption under reaction conditions, mostly through the water gas shift reaction (equation 6). Thus ceria as well as the combination of light with temperature has positive effects over almost all steps which render hydrogen precursor species. The activity is maximized for the most active Pt/2.5CeO$_2$TiO$_2$ catalyst (Figs. 8-11). The mentioned effects on surface species can be thus related to the presence of Ce^{3+} species and concomitant oxygen vacancies at the ceria-titania interface.

4. Conclusions

In this work we synthesized ternary Pt-promoted ceria-titania systems and analyzed their activity for the production of hydrogen from methanol through a thermo-photo catalytic process. The ternary materials contain ceria loading from ca. 1 to 5 wt% and (1 wt%) Pt nanoparticles. The Pt nanoparticles with an average primary particle size of 3.4–3.9 nm are rather similar among ternary samples and also the Pt/TiO$_2$ reference. The ceria nanoparticles have a decreasing fraction of reduced Ce (Ce^{3+}) with the lanthanide content of the ternary powders. The reduced Ce fraction is maximized for a ceria content corresponding
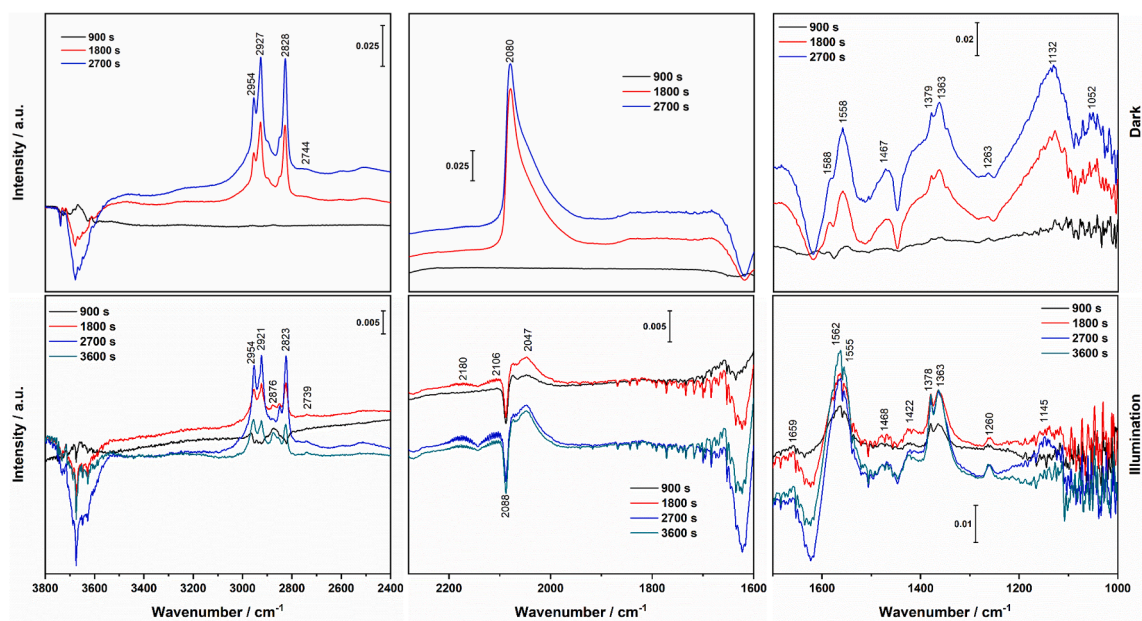
Fig. 10. DRIFT In situ spectra obtained under reaction conditions at 240 °C with the Pt/2.5CeO$_2$TiO$_2$ sample: dark (top panel) and illumination (bottom panel) conditions.
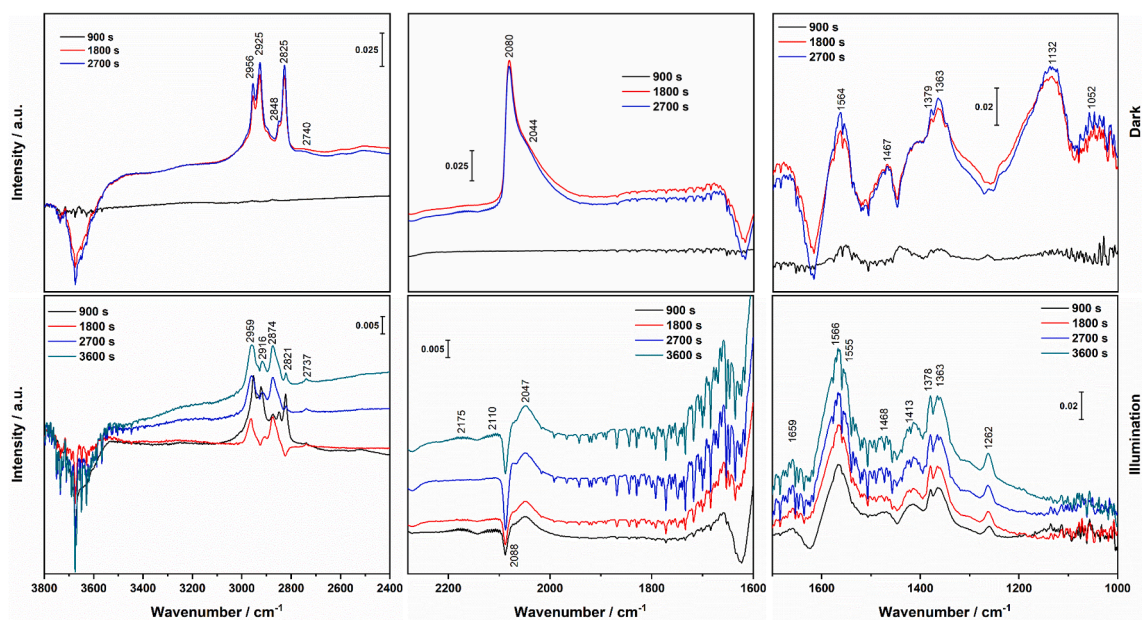

Fig. 11. DRIFT In situ spectra obtained under reaction conditions at 240 °C with the Pt/5CeO$_2$TiO$_2$ sample: dark (top panel) and illumination (bottom panel) conditions.

to the sample presenting maximum activity, the Pt/2.5CeO$_2$TiO$_2$ catalyst. Therefore, this sample displays the optimum ceria-titania interface, high and stable activity in the thermo-photo production of hydrogen, and, particularly, a strong synergy between light and heat energy sources. The synergistic effect was rigorously measured using excess functions and energy balance, reaching the maximum at 240 °C. The data demonstrated an excess output of about 50% from the additive result of light and heat, the highest up to now reported in this reaction.

The in-situ study of the materials shows the stability of the metallic and ceria components under reaction conditions for the most active Pt/2.5CeO$_2$TiO$_2$ catalyst. Absence of structural/electronic changes in all components of the mentioned solid under illumination or by the increase of the temperature was demonstrated using X-ray absorption

techniques, together with microscopy and other (ex-situ) tools. The reaction mechanism was elucidated using in-situ infrared and combines a reforming-type sequential oxidation of the carbon-containing moieties (starting with methanol) with decarbonylation of specific (aldehyde and carboxylate-type) intermediates and the water gas shift reaction. Ceria and the combination of light and temperature are able to promote effectively almost all reaction steps (equations 1–6) rendering the precursor entities of hydrogen and, therefore, boosting the production of this molecule.

Declaration of Competing Interest

The authors declare that they have no known competing financial

interests or personal relationships that could have appeared to influence the work reported in this paper.

Acknowledgments

Appendix A. Supplementary data

Supplementary data to this article can be found online at https://doi.org/10.1016/j.cej.2021.130641.

References

[1] P. Lanzafame, S. Perathoner, G. Centi, S. Gross, E.J.M. Hensen, Grand challenges for catalysis in the science and technology roadmap on catalysis for Europe: moving ahead for a sustainable future, Catal. Sci. Technol. 7 (2017) 5182–5194, https://doi.org/10.1039/C7CY01067B.

[2] H. Olivier-Boubigou, et al., The pivotal role of catalysis in france: selected examples of recent advances and future prospects, ChemCatChem 9 (2017) 2029–2064, https://doi.org/10.1002/cctc.201700426.

[3] A. Kubacka, M. Fernández-García, G. Colón, Advanced nanoarchitectures for solar photocatalytic applications, Chem. Rev. 112 (2012) 1555–1614, https://doi.org/10.1021/cr100454n.

[4] J.C. Colmenares, R. Luque, Heterogeneous photocatalytic nanomaterials: Prospects and challenges in selective transformations of biomass-derived compounds Chem, Soc. Rev. 43 (2014) 765–778, https://doi.org/10.1039/C3CS60262A.

[5] M. Ghoussoub, M. Xia, P.N. Duchesne, D. Segal, G. Ozin, Principles of photothermal gas-phase heterogeneous CO2 catalysis, Energ. Environ. Sci. 12 (2019) 1122–1142, https://doi.org/10.1039/C8EE02790K.

[6] V. Nair, M. Muñoz-Batista, M. Fernández-García, R. Luque, J.C. Colmenares, Thermo-photocatalysis: Environmental and energy applications, ChemSusChem 12 (2019) 2098–2116, https://doi.org/10.1002/cssc.201900175.

[7] Y. Zhou, D.E. Doronkin, Z. Zhao, P.N. Plessow, J. Jlic, B. Detlefs, T. Pruessmann, F. Studt, J.-D. Grunwaldt, Photothermal catalysis over nonplasmonic Pt/TiO2 studied by operando HERFD-XANES, resonant XES, and DRIFTS, ACS Catal. 8 (2018) 11398–11406, https://doi.org/10.1021/acscatal.8b03724.

[8] R. Verma, S.K. Samdarshi, S. Bojja, S. Paul, B. Choudhury, A novel thermophotocatalyst of mixed-phase cerium oxide (CeO2/Ce2O3) homocomposite nanostructure: Role of interface and oxygen vacancies, Sol. Energy Mater. Sol. Cells 141 (2015) 414–422, https://doi.org/10.1016/j.solmat.2015.06.027.

[9] M.J. Muñoz-Batista, A.M. Eslava-Castillo, A. Kubacka, M. Fernández-García, Thermo-photo degradation of 2-propanol using a composite ceria-titania catalyst: Physico-chemical interpretation from a kinetic model, Appl. Catal. B 225 (2018) 298–306, https://doi.org/10.1016/j.apcatb.2017.11.073.

[10] M. Bellardita, R. Fiorenza, L. D̛Urso, L. Spitaleri, A. Gulion, G. Compagnini, S.Scire, L. Palmisano. Exploring the Photothermo-Catalytic Performance of Brookite TiO2-CeO2 Composites. Catalysts 10 (2020) 765-778. 10.3390/catal10070765.

[11] W. Ji, T. Slem, J. Kong, Y. Tong, Synergistic performance between visible-light photocatalysis and thermocatalysis for VOCs oxidation over robust Ag/F-codoped SrTiO3, Ind. Eng. Chem. Res. 57 (2018) 12766–12773, https://doi.org/10.1021/acs.iecr.8b02873.

[12] J.-J. Li, E.-Q. Yu, S.-C. Cai, X. Chen, J. Chen, H.-P. Jia, Y.-J. Xu, Noble metal free, CeO2/LaMnO3 hybrid achieving efficient photo-thermal catalytic decomposition of volatile organic compounds under IR light, Appl. Catal. B 240 (2019) 141–152, https://doi.org/10.1016/j.apcatb.2018.08.069.

[13] S. Fang, Z. Sun, Y.H. Hu, Insights into the thermo-photo catalytic production of hydrogen from water on a low-cost NIOX-loaded TIO2 catalyst, ACS Catal. 9 (2019) 5047–5056, https://doi.org/10.1021/acscatal.9b01110.

[14] M. Bellardita, R. Fiorenza, L. D̛Urso, L. Spitaleri, A. Gulion, G. Compagnini, S.Scire, L. Palmisano. Catalytic and Photothermo-catalytic Applications of TiO2-CoOx Composites. J. Photocatal. 1 (2020) 3-15. 10.2174/2665976X01666200219113505.

[15] A. Caravaca, H. Dayli, M. Smith, A. Mills, S. Chansai, C. Hardacre Continuous flow gas phase photoreforming of methanol at elevated reaction temperatures sensitised by Pt/TiO2. Res. Chem. Eng. 1 (2016) 649-657. 10.1039/C6RE00140H.

[16] U. Caudillo-Flores, G. Agostini, C. Marini, A. Kubacka, M. Fernández-García, Hydrogen thermo-photo production using Ru/TiO2: Heat and light synergistic effects, Applied Catalysis B: Environmental 256 (2019) 117790, https://doi.org/10.1016/j.apcatb.2019.117790.

[17] G. Colón, A. López-Martín, F. Platero, A. Caballero, Thermo-Photocatalytic methanol reforming for hydrogen production over a CuPd−TiO2 catalyst, ChemPhotoChem 4 (2020) 630–637, https://doi.org/10.1002/cptc.202000010.

[18] Y. Nishijima, K. Ueno, Y. Kotake, K. Murakoshi, H. Inoue, H. Misawa, Near-infrared plasmon-assisted water oxidation, J. Phys. Chem. Lett. 3 (2012) 1248–1252, https://doi.org/10.1021/jz3003316.

[19] X. Zhang, X. Ke, J. Yao, Recent development of plasmon-mediated photocatalysts and their potential in selectivity regulation, J. Mater. Chem. A 6 (2018) 1941–1966, https://doi.org/10.1039/C7TA10375A.

[20] R. Ma, J. Sun, D.H. Li, J.J. Wei, Review of synergistic photo-thermo-catalysis: Mechanisms, materials and applications, Int. J. Hydrog. Ener. 45 (2020) 30288–30324, https://doi.org/10.1016/j.ijhydene.2020.08.127.

[21] M. Mao, Q. Zhang, Y; Yang, Y. Li, H. Huang, Z. Jiang, Q. Hu, X. Zhao, Solar-light-driven CO2 reduction by methane on Pt nanocrystals partially embedded in mesoporous CeO2 nanorods with high light-to-fuel efficiency, Green Chem. 20 (2018) 2857-2869. 10.1039/c8gc01058g.

[22] L.V. Mattos, G. Jacobs, B.H. Davis, F.B.H. Noronha, Production of hydrogen from ethanol: Review of reaction mechanism and catalyst deactivation, Chem. Rev. 112 (2012) 4094–4123, https://doi.org/10.1021/cr2000114.

[23] P. Tahay, Y. Khani, M. Jabari, F. Bahadoran, N. Safari, Highly porous monolith/TiO2 supported Cu, Cu-Ni, Ru, and Pt catalysts in methanol steam reforming process for H2 generation, Appl. Catal. A 554 (2018) 44–53, https://doi.org/10.1016/j.apcata.2018.01.022.

[24] G. Gu, J. Long, L. Fan, L. Chen, L. Zhao, H. Lin, X. Wang, Single-site Sn-grafted Ru/TiO2 photocatalysts for biomass reforming: Synergistic effect of dual co-catalysts and molecular mechanism, J. Catal. 303 (2013) 141–155, https://doi.org/10.1016/j.jcat.2013.03.014.

[25] W. Ouyang, M.J. Muñoz-Batista, A. Kubacka, R. Luque, M. Fernández-García, Enhancing photocatalytic performance of TiO2 in H2 evolution via Ru co-catalyst deposition, Appl. Catal. B 238 (2018) 434–443, https://doi.org/10.1016/j.apcatb.2018.07.046.

[26] Wang, H. Liu, Y: Li, R. Yang, Z. Zhang, X. Wang, H. Liu. Hybrid nanostructures of pit-rich TiO2 nanocrystals with Ru loading and N doping for enhanced solar water splitting Chem. Comm. 55 (2019) 2781-2784. 10.1039/C8CC10093D.

[27] A.V. Puga, Photocatalytic production of hydrogen from biomass-derived feedstocks, Coord. Chem. Rev. 315 (2016) 1–66, https://doi.org/10.1016/j.ccr.2015.12.009.

[28] V. Kumaravel, S. Matthew, J. Barlett, S.C. Pillai, Photocatalytic hydrogen production using metal doped TiO2: A review of recent advances, Appl. Catal. B 244 (2019) 1021–1064, https://doi.org/10.1016/j.apcatb.2018.11.080.

[29] J.B. Park, J. Graciani, J. Evans, S. Senanayake, J. Hrbek, J.A. Rodriguez, High catalytic activity of Au/CeOx/TiO2(110) controlled by the nature of the mixed-metal oxide at the nanometer level, J. Proc. Nat. Acc. Sciences 106 (2009) 4975–4980, https://doi.org/10.1073/pnas.0812604106.

[30] A. Bruix, J.A. Rodriguez, P.J. Ramírez, S.D. Senanayake, J. Evans, J.B. Park, D. Stacchiola, P. Liu, J. Hrbek, F. Illas, A new type of strong metal–support interaction and the production of H2 through the transformation of water on Pt/CeO2(111) and Pt/CeOx/TiO2(110) Catalysts, J. Am. Chem. Soc. 134 (2012) 8968–8974, https://doi.org/10.1021/ja302070k.

[31] S. Kundu, J. Ciston, S.D. Senanayake, D.A. Arena, E. Fujita, D. Stacchiola, L. Barrio, R.M. Navarro, J.L.G. Fierro, J.A. Rodriguez, Exploring the structural and electronic properties of pt/ceria-modified TiO2 and its photocatalytic activity for water splitting under visible light, J. Phys. Chem. C 116 (2012) 14062–14070, https://doi.org/10.1021/jp304475x.

[32] M.J. Muñoz-Batista, M.N. Gómez-Cerezo, A. Kubacka, D. Tudela, M. Fernández-García, Role of interface contact in CeO2–TiO2 photocatalytic composite materials, ACS Catal. 4 (2014) 63–72, https://doi.org/10.1021/cs400878b.

[33] M. Zeng, Y. Li, M. Mao, J. Bai, L. Ren, X. Zhao. Synergetic effect between photocatalysis on TiO2 and thermocatalysis on CeO2 for gas-phase oxidation of benzene on TiO2/CeO2 nanocomposites.ACS Catal. 5 (2015) 3278-3286. 10.1021/acscatal.5b00292.

[34] J.J. Plata, E. Rodríguez-Alonso, J. Graciani, A.M. Márquez, J.A. Rodriguez, J. Fernández-Sanz, Understanding the photocatalytic properties of Pt/CeOx/TiO2: Structural effects on electronic and optical properties, ChemPhysChem. 20 (2019) 1624–1629.

[35] M.J. Muñoz-Batista, D. Motta Meira, G. Colón, A. Kubacka, M. Fernández-García, Phase-Contact engineering in mono- and bimetallic Cu-Ni co-catalysts for hydrogen photocatalytic materials, Angew. Chem. Int. Ed. 57 (2018) 1199–1203, https://doi.org/10.1002/anie.201709552.

[36] S.E. Braslavsky, A.M. Braun, A.E. Cassano, A.V. Emeline, M.I. Litter, L. Palmisano, V.N. Parmon, N. Serpone. Glossary of terms used in photocatalysis and radiation catalysis (IUPAC Recommendations 2011). Pure Appl. Chem. 83 (2011) 931-1014. https://doi.org/10.1351/PAC-REC-09-09-36.

[37] H. Zhang, J.F. Banfield, Understanding polymorphic phase transformation behavior during growth of nanocrystalline aggregates: Insights from TiO2, J. Phys. Chem. B 104 (2000) 3481–3487, https://doi.org/10.1021/jp000499j.

[38] A. Kubacka, G. Colón, M. Fernández-García, Cationic (V, Mo, Nb, W) doping of TiO2–anatase: A real alternative for visible light-driven photocatalysts, Catal. Today. 143 (2009) 286–292, https://doi.org/10.1016/j.cattod.2008.09.028.

[39] T. Montini, M. Melchionna, M. Monai, P. Fornasiero, Fundamentals and catalytic applications of CeO2-based materials, Chem. Rev. 116 (2016) 5987–6041, https://doi.org/10.1021/acs.chemrev.5b00603.

[40] S. Loridant, Catal. Today (2020), https://doi.org/10.1016/j.cattod.2020.03.044.

[41] B.M. Reddy, A. Khan, P. Lakshmanan, M. Aouine, S. Loridant, J.-C. Volta, Structural characterization of nanosized CeO2-SiO2, CeO2-TiO2, and CeO2-ZrO2

catalysts by XRD, Raman, and HREM techniques, J. Phys. Chem. B 109 (2005) 3355–3363, https://doi.org/10.1021/jp045193h.

[42] L. Piccolo, P. Afanasiev, F. Morfin, T. Len, C. Dessal, J.L. Rousset, M. Aouine, F. Bourgain, A. Aguilar-Tapia, O. Proux, Y. Chen, L. Soler, J. Llorca, Operando X-ray absorption spectroscopy investigation of photocatalytic hydrogen evolution over ultradispersed Pt/TiO2 catalysts, ACS Catal. 10 (2020) 12696–12705, https://doi.org/10.1021/acscatal.0c03464.

[43] M. Fernandez-García, XANES analysis of catalytic systems´ under reaction conditions, Catal. Rev. Sci. Eng. 44 (2002) 59–121, https://doi.org/10.1081/CR-120001459.

[44] A. Jentys, Estimation of mean size and shape of small metal particles by EXAFS, Phys. Chem. Chem. Phys. 1 (1999) 4059–4063, https://doi.org/10.1039/A904654B.

[45] J. El Fallah, S. Boujana, H. Dexpert, A. Kiennemann, J. Majerus, O. Touret, F. Villain, F.; F. Le Normand. Redox processes on pure ceria and on Rh/CeO2 catalyst monitored by X-Ray absorption (Fast Acquisition Mode). J. Phys. Chem. 98 (1994) 5522−5533. 10.1021/j100072a020.

[46] A. Yamakata, T.-A. Ishibashi, H. Onishi, Electron- and Hole-capture reactions on Pt/TiO2 photocatalyst exposed to methanol vapor studied with time-resolved infrared absorption spectroscopy, J. Phys. Chem. B 106 (2002) 9122–9125, https://doi.org/10.1021/jp025993x.

[47] P.A. Panatoyov, S.T. Burrows, J.P. Morris, Infrared spectroscopic studies of conduction Band and trapped electrons in UV-photoexcited, H-atom n-doped, and thermally reduced TiO2, J. Phys. Chem. C 116 (2012) 6623–6635, https://doi.org/10.1021/jp2053103.

[48] L. Mino, G. Spoto, A.M. Ferrari, CO2 capture by TiO2 anatase surfaces: A combined DFT and FTIR Study, J. Phys. Chem. C 118 (2014) 25016–25026, https://doi.org/10.1021/jp507443k.

[49] G Halasi, G. Schubert, F. Solymosi, Photocatalytic decomposition of methylformate over Pt metals. J. Phys. Chem. C 294 (2012) 199-1206. https:// doi.org/10.1021.jp406840n.

[50] C.E. Nanayakkara, J.K. Dillon, V.CH. Grassian. Surface adsorption and photochemistry of gas-phase formic acid on TiO2 nanoparticles: the role of adsorbed water in surface coordination, adsorption kinetics, and rate of photoproduct formation. J. Phys. Chem. C 118 (2014) 2548-25495. 10.1021/jp507551y.

[51] M. Keulmans, S.W. Verbruggen, B. Haucheme, J.A. Martens, S. Lenaerts, Activity versus selectivity in photocatalysis: morphological or electronic properties tipping the scale, J. Catal. 344 (2016) 221–228, https://doi.org/10.1016/j.jcat.2016.09.033.

[52] M- El-Roz, Ph. Bazin, M. Daturi, F. Thribault-Starzyk. On the mechanism of methanol photo-xodiation to methylformate and CO2 on TiO2. PCCP 17 (2015) 11277. 25495 10.1039/c5ip00726p.

[53] P. Hollins, The influence of surface defects on the infrared spectra of adsorbed species, Surf. Sci. Rep. 16 (1992) 51–94, https://doi.org/10.1016/0167-5729(92)90008-Y.

[54] C. Lentz, S.P. Jand, J. Melke, C. Roth, P. Kaghazchi, DRIFTS study of CO adsorption on Pt nanoparticles supported by DFT calculations, J. Mol. Cata. A 426 (2017) 1–9, https://doi.org/10.1016/j.molcata.2016.10.002.

[55] L. Mino, G. Spoto, S. Bordiga, A. Zecchina, Rutile surface properties beyond the single crystal approach: New insights from the experimental investigation of different polycrystalline samples and periodic DFT calculations, J. Phys. Chem. C 117 (2013) 11186–11196, https://doi.org/10.1021/jp401916q.

[56] M.J. Muñoz-Batista, M.M. Ballari, A. Kubacka, O.M. Alfano, M. Fernández-García, Braiding kinetics and spectroscopy in photo-catalysis: the spectro-kinetic approach, Chem. Soc. Rev. 48 (2019) 637–682, https://doi.org/10.1039/C8CS00108A.

[57] M. Ismael. A review and recent advances in solar-to-hydrogen energy conversion based on photocatalytic water splitting over doped-TiO2 nanoparticles. Solar Energ. 211 (2020) 522.546. 10.1016/j.solener.2020.09.073.

[58] C.-W. Huang, B.-S. Nguyen, J.C.-S. Wu, V.-H. Nguyen, A current perspective for photocatalysis towards the hydrogen production from biomass-derived organic substances and water, Int. J. Hydrog. Ener. 45 (2020) 18144–18159, https://doi.org/10.1016/j.ijhydene.2019.08.121.

[59] O. Fontelles-Carceller, M.J. Muñoz-Batista, E. Rodríguez-Castellón, J.C. Conesa, M. Fernández-García, A. Kubacka, Measuring and interpreting quantum efficiency for hydrogen photoproduction using Pt-titania catalysts, J. Catal. 347 (2017) 157–169, https://doi.org/10.1016/j.jcat.2017.01.012.

[60] G.M. Haselmann, B. Baumgartner, J. Wang, K. Wieland, T. Gupta, Ch. Herzig, A. Limbeck, B. Lendl, D. Elder, In situ Pt photodeposition and methanol photooxidation on Pt/TiO2: Pt-loading-dependent photocatalytic reaction pathways studied by liquid-Phase infrared spectroscopy, ACS Catal. 10 (2020) 2964–2977, https://doi.org/10.1021/acscatal.9b05588.

[61] L. Wang, H. Yue, Z. Hua, H. Wang, X. Li, L. Li, Highly active Pt/NaxTiO2 catalyst for low temperature formaldehyde decomposition, Appl. Catal. B 219 (2017) 301–313, https://doi.org/10.1016/j.apcatb.2017.07.073.

[62] M.J. Muñoz-Batista, A. Kubacka, A.B. Hungría, M. Fernández-García, Heterogeneous photocatalysis: Light-matter interaction and chemical effects in quantum efficiency calculations, J. Catal. 330 (2015) 154–166, https://doi.org/10.1016/j.jcat.2015.06.021.